IEEE Access
Multidisciplinary | Rapid Review | Open Access Journal

Received December 31, 2019, accepted January 7, 2020, date of publication January 13, 2020, date of current version January 29, 2020.

Digital Object Identifier 10.1109/ACCESS.2020.2966363

Investigation of Impacts of Wind Source Dynamics and Stability Options in DC Power Systems With Wind Energy Conversion Systems

AHMED M. I. MOHAMAD[1], MOHAMMADREZA FAKHARI MOGHADDAM ARANI[1], (Member, IEEE), AND YASSER ABDEL-RADY I. MOHAMED[2], (Senior Member, IEEE)

[1]Electrical and Computer Engineering Department, University of Alberta, Edmonton, AB T6G 2V4, Canada
[2]Electrical and Computer Engineering Department, Ryerson University, Toronto, ON M5B 2K3, Canada

Corresponding author: Ahmed M. I. Mohamad (ammohama@ualberta.ca)

This work was supported by the Future Energy Systems Research through Canada First Research Excellence Fund (CFREF).

ABSTRACT Wind energy conversion systems (WECSs), based on permanent magnet synchronous generators (PMSGs), are becoming common sources in dc grids. However, in previous dc grids integration studies, turbine-generator mechanical dynamics are represented by a single-mass model. A practical direct-drive connection in a PMSG-WECS yields lightly-damped torsional speed oscillations because of the double-mass mechanical nature of the generator and the wind turbine. Active damping strategies are usually employed to suppress the mechanical oscillations in a full back-to-back converter interfacing PMSG-WECSs into ac grids; nevertheless, the active damper performance in dc grids is unknown, particularly under dc grid uncertainties and, more importantly, the presence of dynamic and constant power loads commonly used in dc grids. To fill out this gap, this paper presents a detailed modeling and comprehensive stability assessment of a dc grid with a high penetration level of wind power generation. Moreover, stability enhancement strategies are proposed to increase the damping of the entire system, considering different operating and installation scenarios that might face a system integrator/designer. Time-domain simulation studies, based on nonlinear models, are conducted to validate the analytical results. Furthermore, hardware-in-loop real-time simulation studies demonstrate the feasibility of hardware implementation.

INDEX TERMS Active damping, constant power load, dc grid, permanent-magnet synchronous generator (PMSG), stability enhancement, wind power.

I. INTRODUCTION

DC grids (e.g., dc microgrids and dc distribution systems) have gained widespread acceptance in modern distribution systems because of their simple control and economical operation [1], [2]. Furthermore, dc grids facilitate the integration of renewable energy resources into an existing ac network to enhance system reliability and stability. Direct-drive wind energy conversion systems based on permanent magnet synchronous generators (PMSGs) have become preferable because of their several merits, such as the elimination of the gearbox, high power density, and reduced losses.

Wind power generators can be directly interfaced to a dc grid via a voltage-source converter (VSC) to supply energy to dc loads or the main ac grid with the back-to-back configuration [3]–[6]. The integration of wind generators in dc grid can be challenging if the penetration level of wind power generation is high, and the detailed dynamics of the wind turbine system are considered. In dc systems literature, the wind turbine-generator dynamics are likely represented by a single-mass model. However, it has been shown that a practical direct-drive PMSG can exhibit mechanical resonance because of the double-mass mechanical nature of the generator and wind turbine. Further, it has been reported that using the single-mass model can lead to an incorrect and deceptive assessment of the system dynamics [7]–[13].

The mechanical resonance phenomenon is significant when the generator shaft becomes soft. The drive train torsional characteristics can lead to lightly damped speed oscillations if the system is excited by a mechanical or an electrical disturbance, resulting in fluctuations in the output power. The frequency of the oscillation is typically in the

The associate editor coordinating the review of this manuscript and approving it for publication was Zhilei Yao.

low-frequency range (1–70 rad/s), which might lead to further stability problems in dc grids fed by PMSG-based WECSs, where the dynamics of dc grids are significant (dominant) in the low-frequency range. An active damper is usually adopted to suppress the mechanical oscillations developed and avoid the associated instabilities. The PMSG controller can be equipped with active damping strategies to increase the positive damping of the mechanical dynamics, based on the energy stored in the dc-link capacitors of the back-to-back converters [7]–[13]. However, the performance of the PMSG stabilization loops in dc systems is unknown and needs further investigation.

A lot of work has been conducted to address the stability problems that arise in dc grids; however, the stability enhancements focused on mitigating the instability problems caused by the constant power load [14]–[19]. Alternatively, active damper units have been widely used in dc systems, where an auxiliary converter has been employed to mitigate the instabilities caused by CPLs and to improve the system response during start-up and fault conditions [20]–[24]. However, the effectiveness of these stabilization methods to mitigate the instabilities caused by the wind generator mechanical dynamics in dc grids has not been yet investigated.

Based on the above discussion, it is obvious that comprehensive studies on the detailed modeling and stability assessment of the interaction dynamics of a wind turbine generator in dc systems are lacking in the current literature. Moreover, dc grids stability enhancement solutions that could deal with the newly developed interactions are not fully investigated and validated. Therefore, the contributions of this paper can be highlighted as follows:

- Developing detailed small-signal models and stability assessment method of the interaction dynamics of a typical dc grid, considering the double-mass mechanical dynamics of the wind turbine generator and typical load dynamics of dc grids (e.g., constant power loads and dynamic loads).
- Characterizing the impact of dc system uncertainties (e.g., system parameters and load types) on the functionality of the PMSG pre-installed active damper.
- Proposing stabilization strategies to improve the overall system damping capabilities, considering different installation scenarios.

Detailed theoretical analysis and time-domain simulation results are presented to show the validity and effectiveness of the proposed models and stabilization solutions.

II. SYSTEM MODELING

Fig. 1 shows the configuration of a dc grid under investigation. The system consists of a full-scale PMSG based wind turbine generator interfaced to the dc bus via an ac/dc voltage source converter (*W-VSC*). The dc system exchanges power with the ac utility via a bidirectional ac/dc voltage source converter (*G-VSC*). The dc bus is tied to the load bus via a dc feeder (L_g–R_g), where a composite load and a bus capacitance (C_{BUS}) are connected [3], [25]. At the load bus, a composite load is connected, which is composed of a resistive load, constant power load, and motor-drive load (dynamic load).

The modeling details of the system components (PMSG, ac grid, loads, and dc feeder) and the augmented state-space model are presented in the next subsections. Practical and typical parameters for the system shown in Fig. 1 are given in the Appendix.

A. PMSG MODEL

The PMSG is modeled in a *dq*-reference frame, where the *d*-axis of the is aligned with the rotor flux [26], the stator current (I_{dq}), and the generator terminal voltage (U_{dq}) dynamics are given in (1).

$$U_{dq} = \begin{bmatrix} R_s + sL_d & -\omega_e L_q \\ \omega_e L_d & R_s + sL_q \end{bmatrix} I_{dq} + \begin{bmatrix} 0 \\ \lambda \end{bmatrix} \omega_e \tag{1}$$

The relation between the PMSG electromagnetic torque (T_g), rotor PMSG rotational speed (ω_g), and generator output power (P_g) are given by [8]

$$P_g = T_g \omega_g \tag{2}$$

$$T_g = 1.5P(\lambda I_q + (L_d - L_q) I_d I_q) \tag{3}$$

where ω_e is the generator electrical frequency; R_s, L_{dq}, λ, P are the stator resistance, stator inductances, magnetic flux constant, and number of PMSG poles, respectively.

The PMSG power (P_g) and the injected power to the dc bus (P_{dc}) are related via the W-VSC capacitance (C_g) by [27]

$$P_g - P_{dc} = 0.5 C_g s (V)^2 \tag{4}$$

The mechanical dynamics of the wind turbine is represented by the two-mass model [9], [12] and are given by (5)-(8)

$$\omega_t = \frac{1}{S} \frac{1}{2H_t} (T_t - K_s \theta - D_t \omega_t) \tag{5}$$

$$\theta = \frac{1}{s} \omega_b (\omega_t - \omega_g) \tag{6}$$

$$\omega_g = \frac{1}{S} \frac{1}{2H_g} (K_s \theta - T_g - D_g \omega_g) \tag{7}$$

$$T_t = \frac{P_w}{\omega_t} = \frac{0.5 \rho C_P(\lambda_t, \beta) A v_w^3}{\omega_t} \tag{8}$$

where H_t and H_g are turbine's and generator's inertia constants; T_t and K_s are wind turbine torque, shaft stiffness; D_t and D_g are wind turbine and generator damping factors; θ and ω_t are the shaft angle and wind turbine rotating speed; $\rho, C_P, \beta, A, \lambda_t, V_w$ are the air density, wind turbine power coefficient, pitch angle, turbine blades area, tip ratio, and wind speed, respectively.

With the help of the field-oriented control [19], [20], the *W-VSC* controller is controlled to regulate the dc-link voltage and the PMSG terminal voltage (U) via two conventional PI controllers ($G_{vdc}(s)$, $G_{vac}(s)$) at the outer control loop of the

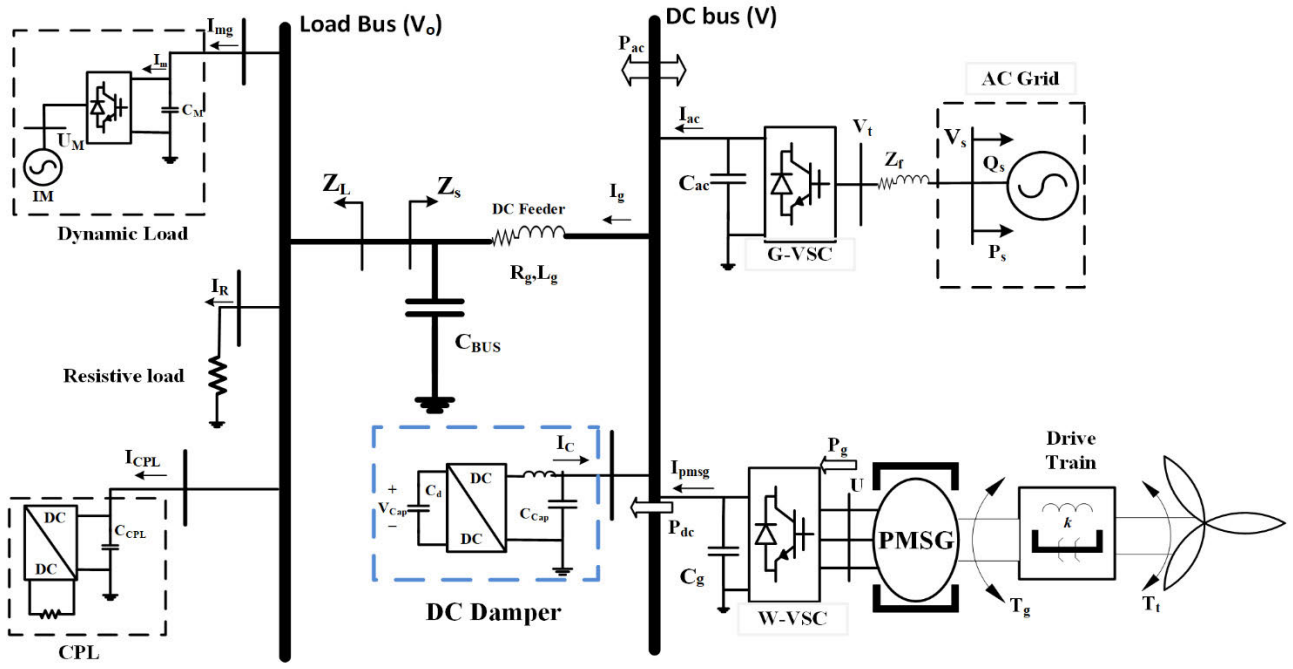

FIGURE 1. DC grid configuration.

W-VSC, as depicted in Fig. 2(a). Two PI current controllers ($G_c(s)$) are adopted to regulate the *W-VSC* currents to their reference values generated by the outer loops, as shown in Fig. 2(a). The PMSG inner loop is equipped with an active damping loop to suppress the mechanical resonance as suggested in [7]–[11]. The active damping loop is realized by feedbacking the PMSG rotational speed (ω_g) to the inner loop via a band-pass filter ($G_{dm}(s)$), and gain (K). The inner and outer loops dynamics are given by

$$I^*_{dm} = \left[G_{vdc}(s)(U^* - U)\right] \tag{9}$$

$$I^*_{qm} = -\left[G_{vac}(s)((V^*)^2 - (V)^2)\right] + KG_{dm}(s)\omega_g \tag{10}$$

$$U^*_d = G_c(s)(I^*_{dm} - I_{dm}) + \omega_e L_q I_{qm} \tag{11}$$

$$U^*_q = G_c(s)(I^*_{qm} - I_{qm}) + \omega_e \lambda - \omega_e L_d I_{dm} \tag{12}$$

B. AC GRID MODEL

The ac grid converter is operated to inject or absorb active power from the dc bus, according to the loading and generation conditions. The bidirectional *G-VSC* inner and outer loop dynamics are shown in Fig. 2(b), the power exchanged at the dc bus (P_{ac}) is regulated via a PI controller ($G_P(s)$) at the outer control loop of the converter at a unity power factor. Two PI current controllers ($G_i(s)$) are adopted to regulate the converter currents to their reference values generated by the outer loop. The ac network model and the *G-VSC* voltage dynamics are given by [29]

$$V_{tdq} = \begin{bmatrix} R_F + sL_F & -\omega L_F \\ \omega L_F & R_F + sL_F \end{bmatrix} I_{dq} + V_{sdq} \tag{13}$$

$$I^*_d = \frac{2}{3V_s}\left[G_P(s)(P^*_{ac} - P_{ac})\right] \tag{14}$$

$$V^*_{td} = G_i(s)(I^*_d - I_d) + V_{sd} - \omega L_F I_q \tag{15}$$

$$V^*_{tq} = G_i(s)(I^*_q - I_q) + V_{sq} + \omega L_F I_d \tag{16}$$

where V_{sdq}, V_{tdq}, and I_{dq} are the d-q components of the ac grid voltage and current in the ac grid reference frame; R_f, and L_f are combined filter and ac grid resistance and inductance; and ω is the ac grid angular frequency, respectively.

C. LOAD MODEL

The currents of the resistive load (R) and the CPL consumed power (P_{CPL}) are given by [30]

$$I_R = \frac{V}{R}, \quad I_{CPL} = \frac{P_{CPL}}{V} \tag{17}$$

A realistic example of a dynamic load (DL) that might exist in dc grids is sensor-less $V/f-$controlled induction motor (IM) drives. The dc current drawn by the dynamic load (I_{mg}) is related to the load bus voltage (V_o) in (18)-(19), further details about the dynamic load are found in [31].

$$I_m = 1.5(m_{sd}I_{sd} + m_{sq}I_{sq}) \tag{18}$$

$$I_{mg} = C_M s V_o + I_m \tag{19}$$

where I_m, I_{sdq}, m_{sdq}, and C_M are the motor drive dc-link current, the IM stator current and the drive duty ratios in an arbitrary reference frame, and the drive's dc link capacitor.

D. DC GRID MODEL

The dynamics of the dc bus and load bus are given by [30]

$$V = V_o + (R_g + sL_g)I_g \tag{20}$$

$$I_{ac} + I_{pmsg} = C_{Bus} s V_o + I_{mg} + I_R + I_{CPL} \tag{21}$$

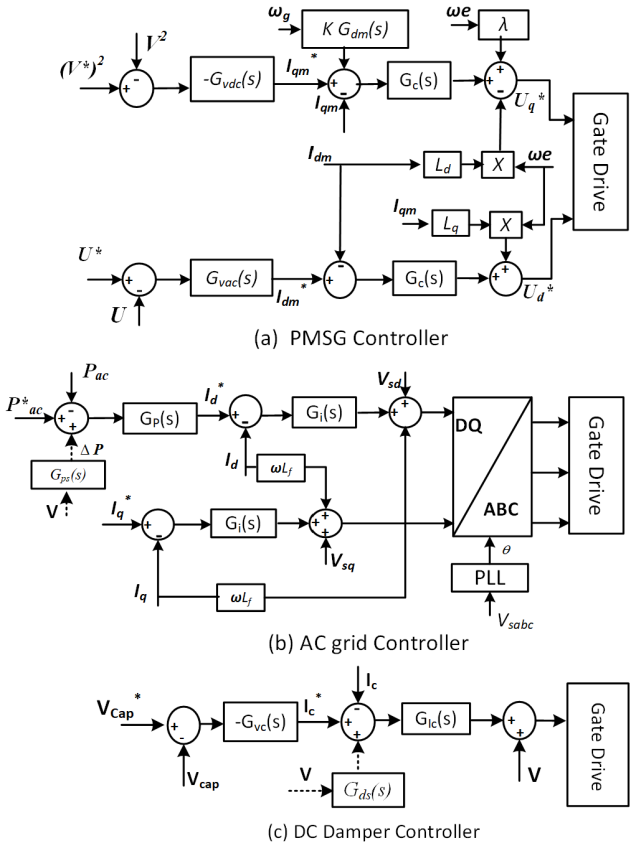

FIGURE 2. Controller diagram of (a) W-VSC. (b) G-VSC. (c) DC Damper.

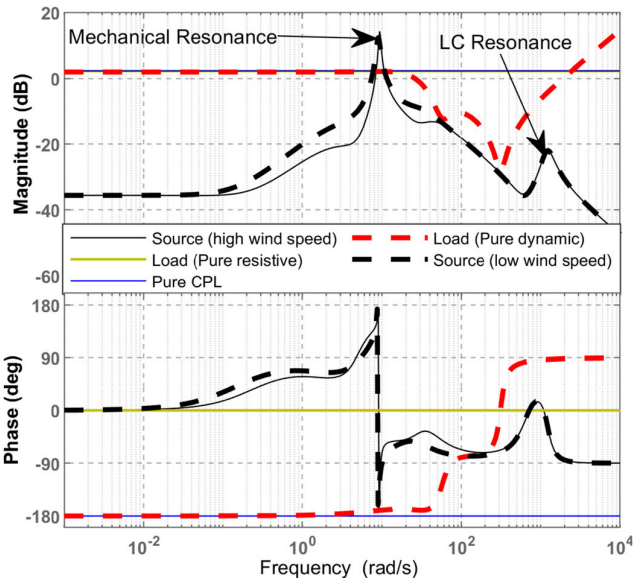

FIGURE 3. Frequency response of the dc grid impedances.

where I_{pmsg} and I_{ac} are the dc currents of the *W-VSC* and *G-VSC*, respectively.

To investigate the overall system dynamics and the stability limits, the small-signal state-space model is developed in (22) by linearizing (1)-(21).

$$\begin{aligned} \dot{\tilde{X}} &= A\tilde{X} + B\tilde{U} \\ \tilde{Y} &= C\tilde{X} + D\tilde{U} \end{aligned} \tag{22}$$

III. STABILITY ASSESSMENT

The entire system stability is assessed with the help of the frequency response of the system small-signal impedances, and the eigenvalues of the state matrix (A) developed in (22). At the dc bus shown in Fig. 1, the PMSG, *W-VSC*, ac gird, *G-VSC*, and their output filters; dc feeders and bus capacitance, are represented by the source impedance (Z_s); whereas a resistive load, a CPL, and a dynamic load are signified by the impedance (Z_L).

The frequency response of the source-side and the load-side impedances at different wind speeds and different load types are plotted in Fig. 3. It is obvious that the source-side impedance includes two peak resonances; the first peak resonance is induced because of the mechanical dynamics of the wind turbine at around 10 rad/s, the resonance peak is associated with almost $\pm 180°$ phase-shift angle, it can be noted that the mechanical resonance peak is independent of the wind speed. The second resonance peak is generated because of the LC network constructed from the dc feeder inductance and the equivalent bus capacitance at the load bus. On the other hand, the resistive load and the CPL are represented by an impedance of constant magnitude and phase-shift angle $0°$ and $-180°$ along the entire frequency range, respectively. The dynamic load shows a constant impedance magnitude and $(-180°)$ phase-shift angle at the very low-frequency range (0-40 rad/s), which resembles the behavior of an ideal constant power load at the low-frequency range. It can be noted that the dynamic load has two significant resonance notches at (50 - 350 rad/s) because of the induction motor rotor and stator circuits [31].

The load-source impedance interactions shown in Fig. 3 result in the system dominant eigenvalues; namely 1) the mechanical eigenvalues (poles), which are induced by the wind turbine generator mechanical dynamics at the low-frequency range; 2) dc grid eigenvalues, which result from the source-load impedance interactions of the dc grid at the low-frequency range; 3) LC resonance eigenvalues at the medium frequency, which result from the interaction between dc gird equivalent LC network and the load impedance; and 4) dynamic load poles that appear in the case of dynamic load existence, as shown in Fig. 4.

Fig. 4(a) shows the system eigenvalues when the load nature changes from a pure resistive to 100% CPL, it is obvious that the entire system poles move towards the right side of the s-plane with increasing CPL penetration level indicating a reduction in the system stability margin. The damping factors of the dominant poles drop from 0.05 to -0.13 pu (mechanical poles), 0.62 to 0.5 pu (dc grid poles), and 0.18 to 0.16 pu (LC resonance poles). However, the mechanical resonance poles are significantly affected by the

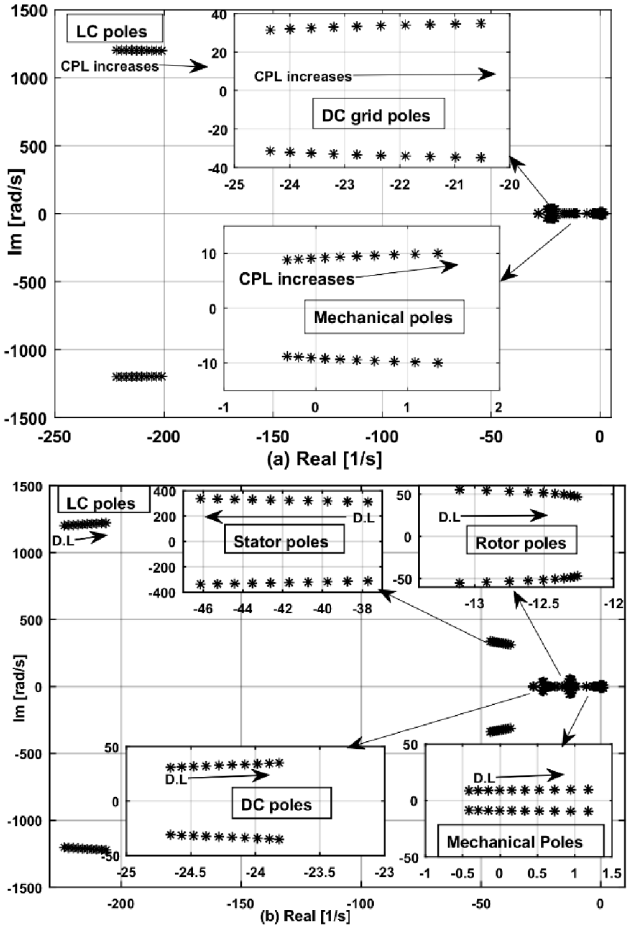

FIGURE 4. System eigenvalues variation against: (a)CPL level, and (b) DL level.

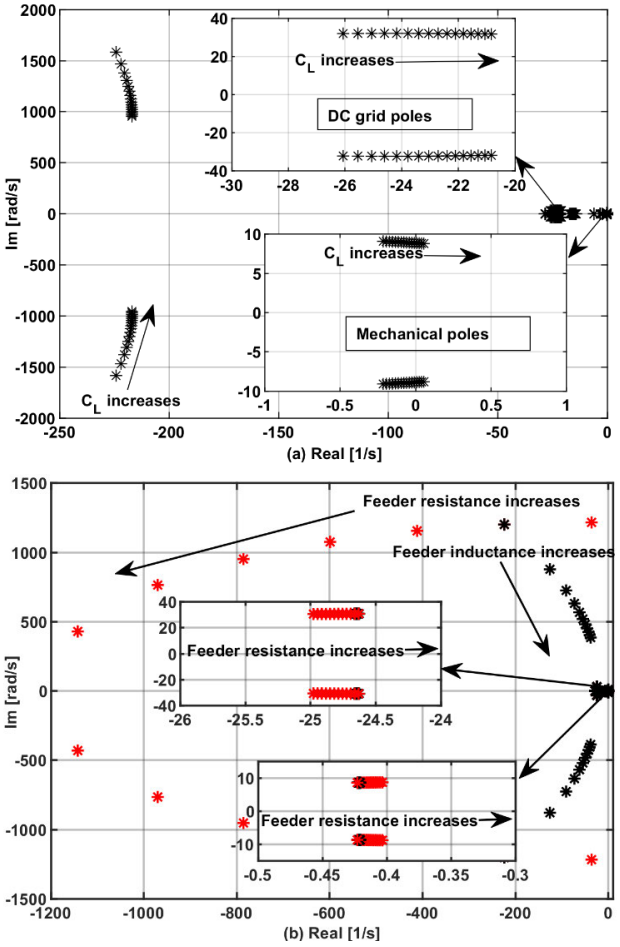

FIGURE 5. System eigenvalues variation against: (a) Load Capacitance and (b) dc feeder parameters.

load nature, where they are located at the $j\omega$-axis when the CPL level is 50% of the total load.

A dynamic load of the same CPL power rating has an almost identical impact on the system dynamics, as depicted in Fig. 4(b), where the damping factors (at 100% dynamic load) drop to -0.134 pu (mechanical poles), 0.55 pu (dc grid poles), 0.165 pu (LC resonance poles), leading to a similar CPL effect at the low-frequency range. On the other hand, the dynamic load induces two well-damped pairs of eigenvalues at the low frequency (45 rad/s) and medium frequency range (350 rad/s), which result from the rotor and stator circuits of the induction motor, respectively. It can be noted that the rotor eigenvalues slightly move toward the right side of the s-plane with increasing the dynamic load penetration level (0.25 pu damping factor at 1 pu), whereas the stator poles move towards the left side of the s-plane (0.13 pu damping factor at 1 pu), indicating a reasonable stability margin of the load eigenvalues.

At 75% resistive load and 25% CPL, the impact of the system uncertainties such as the load bus capacitance (0.5-2 pu), the dc feeder inductance and resistance (0-10 pu), on the system dominant eigenvalues, is presented in Fig. 5(a) and 5(b), respectively. The damping factor of the LC poles increases with the load capacitance (0.14 to 0.22 pu), whereas, the damping factors of the dc grid and the mechanical poles drop from 0.62 to 0.54 pu and 0.03 to -0.006 pu, respectively. However, increasing the load capacitance has a more destabilizing effect on the mechanical poles leading to unstable operation when the bus capacitance is doubled. The variation of the dc feeder inductance and resistance has a negligible effect on the mechanical resonance and dc grid poles, whereas increasing the feeder resistance improves the LC poles damping by pushing them to the left side of the s-plane. On the contrary, increasing the dc feeder inductance significantly reduces the damping factor of the LC poles (0.08 pu). A summary of the conducted sensitivity analysis is provided in TABLE 1.

From the previous analysis, it is clear that the investigated dc system exhibits stability problems with the variation of the system uncertainties, particularly the variation of the connected load nature and the dc bus capacitance. Therefore, effective stabilization strategies are necessary to enhance the

TABLE 1. Sensitivity analysis summary.

Eigenvalues Damping	System Uncertainties increase	Without Proposed Stability Enhancement (Section III)	With Stability Enhancement Methods (Section IV)	
		PMSG Active Damper	AGS	DDE
Mechanical	CPL Level	Causes instability	Unaffected	Varies but always stable
	Bus Cap.	Causes instability	Unaffected	Varies but always stable
DC grid	CPL Level	Decreases but still well damped	Negligible reduction	Decreases but always well damped
	Bus Cap.	Decreases but still well damped	Minor reduction	Decreases but always well-damped
LC network	CPL Level	Decreases	Decreases	Decreases
	Bus Cap.	Increases	Increases	Increases

damping of the poorly damped modes and to ensure robust performance at different operating conditions.

IV. STABILITY ENHANCEMENT

In this section, two stability enhancement strategies are proposed to increase the entire system stability margin. Because the CPL and the dynamic load showed a very close impact on the mechanical poles damping, 100% CPL loading condition has been used in the design of the active stabilizers' loops. The first proposed stability option is realized by modifying the outer loop of the *G-VSC* so that it injects damping power components to stabilize the dc grid. The second stability enhancement method is realized by installing a dc damper at the dc bus, as shown in Fig. 1. The dc damper resembles an active damping resistance, which is tuned to suppress the resonances arising from the load or the source. The second solution is beneficial for a dc system where the stabilization from the ac side is unavailable because of operational or installation reasons.

A. AC GRID SUPPORT(AGS)

The ac grid stability enhancement is realized by injecting a stabilizing component (ΔP) to the reference power command (P^*_{ac}), as shown in Fig. 2(b), where the stabilizing power is obtained by processing the dc bus voltage (V) through the compensator ($G_{ps}(s)$). The stabilizing power component is given in (23).

$$\Delta P = G_{ps}(s)V, \quad G_{ps}(s) = k_{ps}\frac{s}{s+\omega_{ps}} \tag{23}$$

where ω_{ps} and k_{ps} are the gain and the corner frequency of the compensator.

The compensator parameters (ω_{ps} and k_{ps}) are selected to reshape the source impedance (Z_s) so that the intersections with load-side impedance (Z_L) are eliminated at the low-frequency proximity, as demonstrated by the Bode plot portrayed in Fig. 6. The proposed stability enhancement yields a

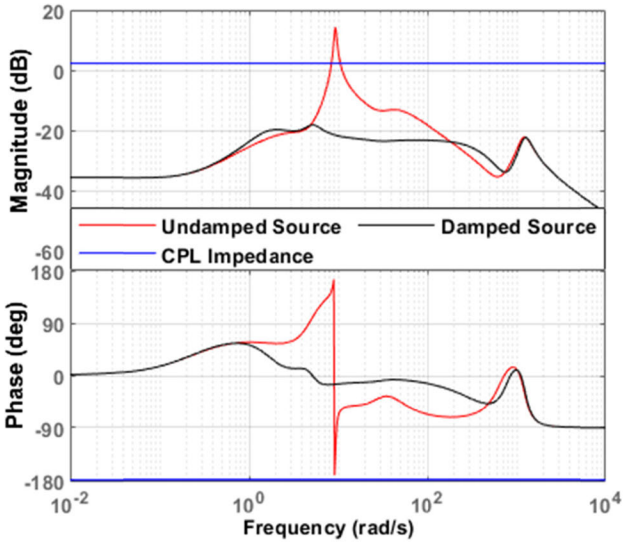

FIGURE 6. System frequency response with AGS strategy.

significant improvement in the damping factor of the mechanical poles, where it increases from −0.13 pu to 0.24 pu at 100% CPL.

The impact of varying the load type on the dominant system eigenvalues with the proposed stability method is illustrated in Fig. 7(a). It can be noted that mechanical poles are two well-damped pairs at the low-frequency range, where their damping factor slightly decreases (0.61 to 0.57 pu and 0.26 to 0.24 pu) when the CPL penetration level is varied from 0 to 100%.

The damping factor of the dc grid poles shows a negligible reduction (0.005 pu), whereas the damping of the LC poles is still sensitive to the load type; however, they are still located at the left side of the s-plane with an acceptable damping factor of 0.15 pu at 100 % CPL.

The impact of varying the load capacitance (0.5-2 pu) on the dominant eigenvalues is shown in Fig. 7(b), where it is

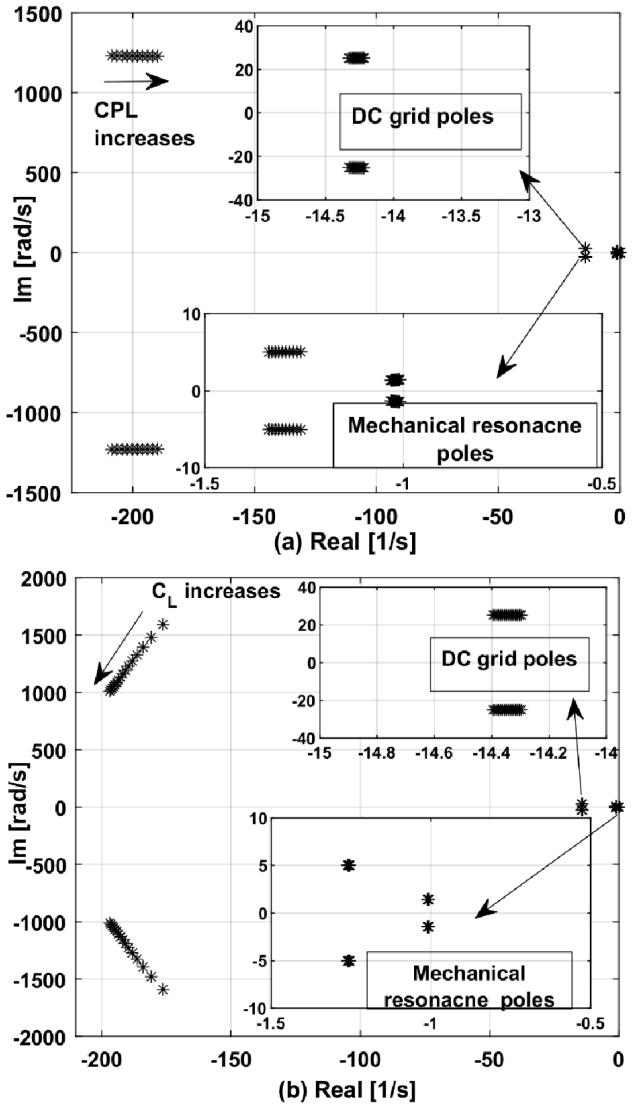

FIGURE 7. Eigenvalues spectrum with AGS against (a) load type and (b) load capacitance.

obvious that the mechanical poles are not affected by the load capacitance uncertainty, whereas the dc grid poles show a minor reduction in their damping factor (0.002 pu). This proves the robustness of the proposed method against the load type and load capacitance. On the other hand, increasing the load capacitance significantly enhances the damping capability of the LC poles, as discussed in the previous section.

B. DC DAMPER ENHANCEMENT (DDE)

Fig.1 shows the structure of the proposed dc damper, where a capacitor (C_d) is interfaced to the dc grid via a dc/dc converter and an output LC filter. Fig. 2(c) shows the controller block diagram of the proposed dc stabilizer, where the dc/dc converter is operated to regulate the capacitor voltage (V_{cap}) to a fixed value ($V_{cap}{}^*$) via two PI compensators ($G_{vc}(s)$ and $G_{Ic}(s)$) at the outer and inner loops, respectively. To mitigate

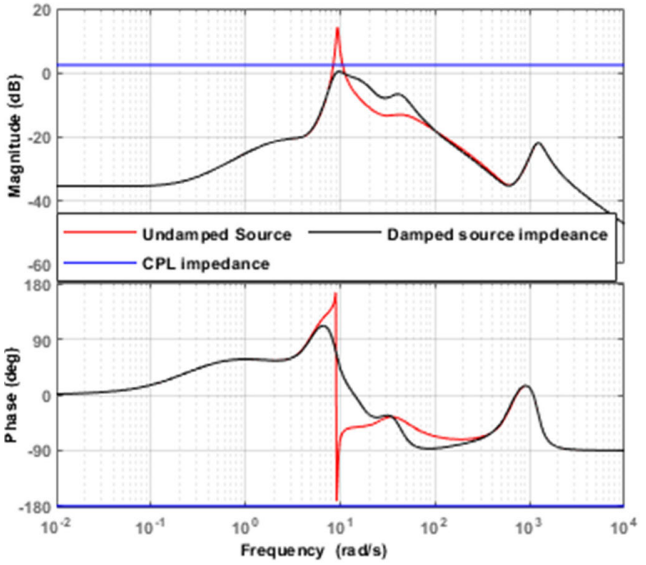

FIGURE 8. System frequency response with DDE strategy.

the instability problem of the dc grid, the dc bus voltage (V) is processed via a second-order compensator ($G_{dc}(s)$), and the output is fed to the inner loop. The compensator parameters of the dc damper given in (24) are selected to eliminate the interactions of the load-source impedance interactions, as depicted in Fig. 8.

Moreover, the compensator gain is chosen to increase the positive damping of the mechanical eigenvalues at 100% CPL condition, where the lowest stability margin is obtained as discussed in Section III.

$$G_{ds}(s) = k_{ds}\frac{2\xi_{ds}\omega_{ds}\mathrm{s}}{s^2 + 2\xi\omega_{ds}\mathrm{s} + \omega_{ds}^2} \tag{24}$$

where $k_{ds}, \xi_{ds,}$ and ω_{ds} are the gain, damping ratio, and the natural frequency of the compensator, respectively.

Based on the previous design approach, the proposed stability enhancement method yields 0.25 pu damping factor for the mechanical and dc grid poles, whereas the LC poles damping factor remains unchanged. Fig. 9(a) demonstrates the impact of the load type on the system dominant eigenvalues. The mechanical poles are two pairs of equal damping factor (0.25 pu) at 100% CPL conditions. One of the mechanical poles pair damping factor increases to 0.45 pu, and the damping factor of the other pair drops to 0.18 pu, when the load is purely resistive, maintaining an acceptable stability margin with the load type variation. The dc poles and LC poles show a similar trend at pure resistive loading, where their damping factor increases by 0.08 pu and 0.02, respectively.

The impact of varying the load capacitance on the dominant eigenvalues is shown in Fig. 9(b), like the load type variation, the mechanical poles show a variation with the load capacitance, where their damping factors change from 0.25 pu to (0.22 pu and 0.27 pu), when the bus capacitance drops to 0.5 pu. On the other hand, the damping of the dc grid and LC poles show an improvement (0.05 pu) when the

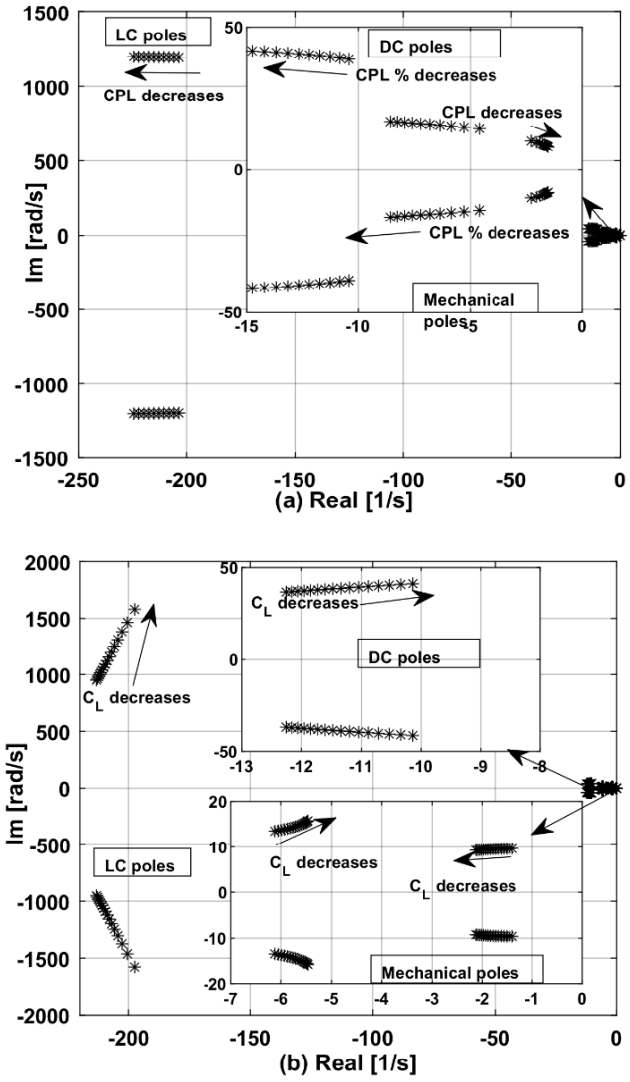

FIGURE 9. Eigenvalues spectrum with DDE against (a) load type and (b) load capacitance.

load capacitance is doubled. A summary of the conducted sensitivity analysis is provided in TABLE 1.

V. SIMULATION RESULTS

Time-domain simulation studies, using the detailed nonlinear models of the system components under the MATLAB/Simulink environment, are conducted to evaluate the performance of the dc grid shown in Fig. 1. Furthermore, the performance of the proposed stability enhancement methods is assessed. The system base values and controller parameters are given in the Appendix.

A. SYSTEM RESPONSE WITHOUT PROPOSED STABILITY ENHANCEMENT METHODS

The dynamic performance of the dc grid under investigation is assessed with only the PMSG active damper. The ac grid injects 0.35 pu active power to the dc grid via the *G-VSC* at a unity power factor, whereas the connected load is 80%

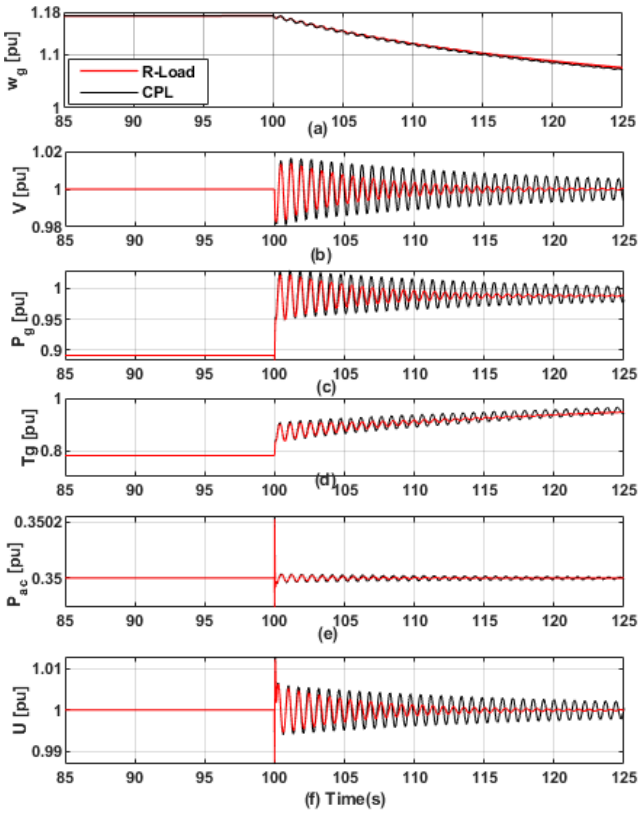

FIGURE 10. System response with PMSG stabilization loop (a) PMSG rotational speed, (b) DC bus voltage, (c) PMSG active power, (d) PMSG Torque, (e) ac grid active power, and (f) PMSG terminal voltage.

resistive and 20% CPL. Fig. 10 compares the system response when a resistive load and CPL (200 kW) are switched at $t = 100$ s, it can be seen that load switching leads to a reduction of the PMSG rotational speed (ω_g) and an increase in the electromagnetic (T_g) torque and active power (P_g). The load switching event is associated with lightly damped mechanical oscillations, which are mapped to the dc grid, leading to an oscillatory performance at the dc bus voltage (V) and the ac grid power (P_{ac}) at the mechanical resonance frequency (10 rad/s). It is evident that the load nature significantly affects the overall system damping capability, where more time is needed to dampen the oscillations produced by CPL switching if compared to the resistive load switching, the obtained simulation results agree with the theoretical analysis conducted in Section III.

B. SYSTEM RESPONSE WITH AC GRID SUPPORT

Fig. 11 presents the impact of the ac grid stability enhancements effort on the dc grid dynamics, where the connected load is set to 100% CPL; the power demand from the ac side is increased by 100 kW at $t = 65$ s, a CPL (200 kW) is switched at $t = 70$ s, and the system is subjected to wind speed variation as shown in Fig. 11(a). It is obvious that the system smoothly responds to the wind speed variation and load switching events with almost an oscillation-free

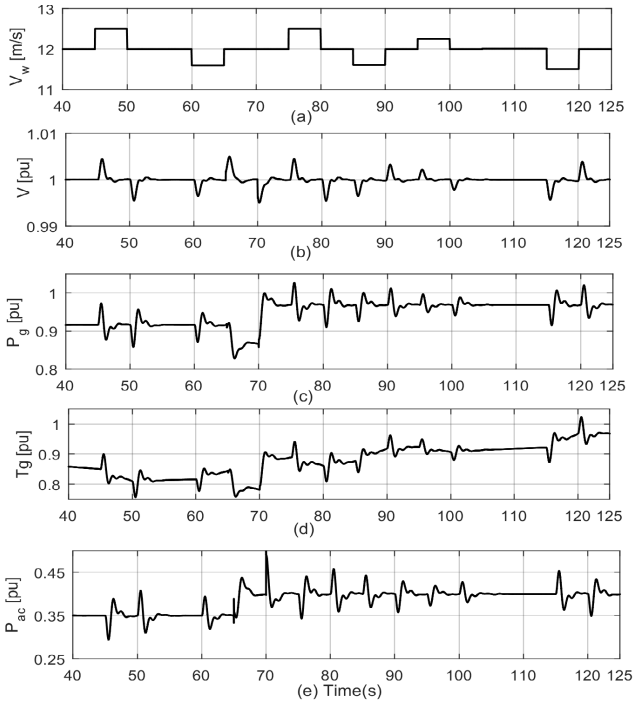

FIGURE 11. System response with AGS method (a) wind speed, (b) DC bus voltage, (c) PMSG active power, (d) PMSG Torque, and (e) ac grid active power.

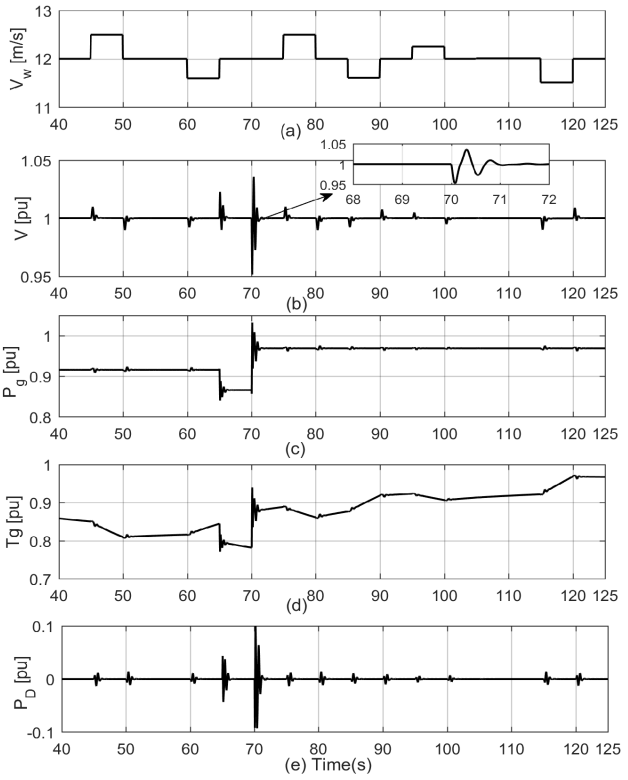

FIGURE 12. System response with DDE method (a) wind speed, (b) DC bus voltage, (c) PMSG active power, (d) PMSG Torque, and (e) dc damper power.

profiles of the PMSG torque and output power. The significant improvement of the PMSG dynamic performance affects the dc-bus voltage and the ac grid power dynamics, where the lightly damped mechanical oscillations are completely suppressed with minimal overshoots (less than ± 1 %) in the dc-link voltage response. Furthermore, it can be observed that remarkable stability enhancement is realized by injecting damping power components by the ac grid via the *G-VSC* when the system is subjected to any disturbance, as demonstrated in Fig. 11(e). The conducted assessment proves the effectiveness proposed stabilizer and its robustness (functionality) against different uncertainties.

C. SYSTEM RESPONSE WITH DC DAMPER

The test employed to examine the functionality of the ac grid support (AGS) is conducted to assess the capability of the dc damper to preserve the overall system stability, as demonstrated in Fig. 12. It is obvious that the dc damper has succeeded to deal with the wind speed variation and the load switching events at 100% CPL operation. The system stability is maintained via the dc damper through injecting a transient stabilizing power (P_D) to the dc system at the instant of voltage fluctuation due to load switching or wind speed variation, where the stabilizing power (P_D) counteracts the power oscillations injected into the dc-bus by the PMSG, as portrayed in Fig. 12(e). Moreover, it can be noted that the dc-bus voltage recovers faster as compared to the AGS enhancement; however, the voltage response exhibits higher overshoot (less than $\pm 5\%$) at the instant of load switching. Further, the improvement of the dc-bus voltage is reflected on the PMSG torque and active power dynamics, which are associated with fewer fluctuations and faster dynamic behavior as compared to the AGS method. It should be pointed out that the AGS method offers higher damping capabilities than the dc damper method although both methods are designed to improve the mechanical damping poles damping factor to the same value (≈ 0.25 pu), this is attributed to the dc poles, which have a higher damping factor with the AGS method. The simulation results confirm the accuracy of the conducted analysis in Section IV.

D. COMPARISON WITH PREVIOUS METHODS

The response of the dc system with the PMSG active damper proposed in [7] is compared to the response of the stability enhancement options proposed in this work. Similar to the active damper given in (10), the PMSG rotational speed is fed-back to the outer loop via a band-pass filter and gain to mitigate the mechanical resonance problem as suggested in [7]. The compensator of this method is designed so that the damping factor of both the mechanical poles and dc grid poles is 0.31 pu at 100% CPL. For the same test employed in Section V-B, Fig. 13 compares the dc grid response with the AGS enhancement method and with the outer loop PMSG

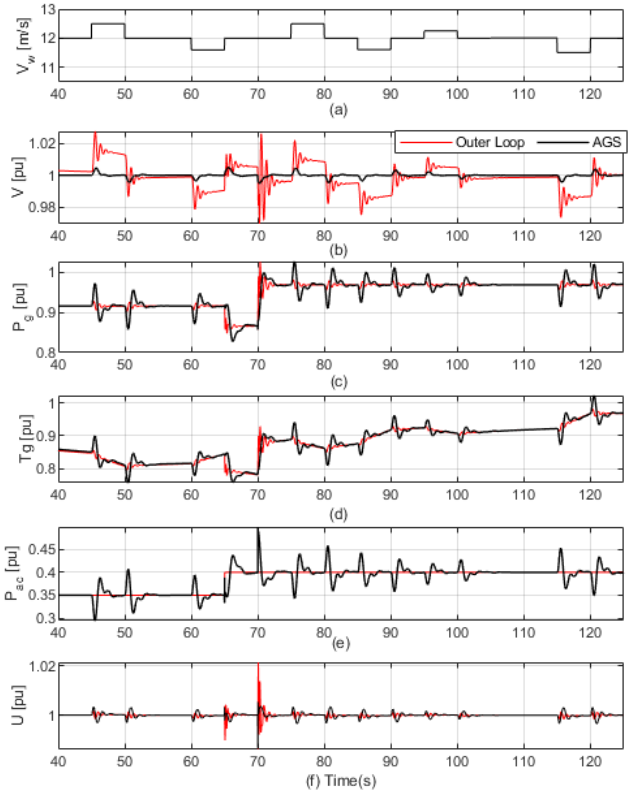

FIGURE 13. Comparison of dc grid response with AGS method and outer loop PMSG active damper (a) wind speed, (b) DC bus voltage, (c) PMSG active power, (d) PMSG Torque, (e) ac grid active power, and (f) PMSG terminal voltage.

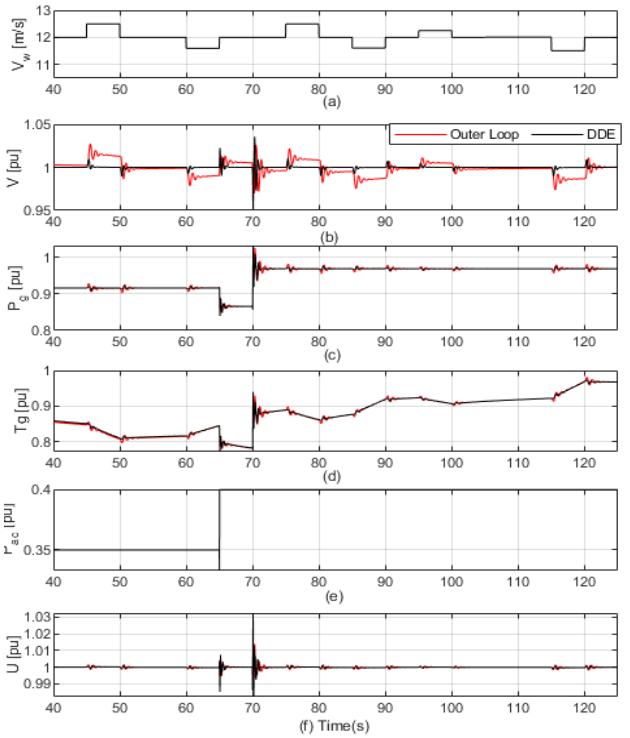

FIGURE 14. Comparison of dc grid response with AGS method and outer loop PMSG active damper (a) wind speed, (b) DC bus voltage, (c) PMSG active power, (d) PMSG Torque, (e) ac grid active power, and (f) PMSG terminal voltage.

damper proposed in [7]. The AGS method shows better dc bus voltage response, where the PMSG damper affects the tracking capability of the dc-link voltage controller, leading to the deviation of the dc-link voltage from its nominal value. Although the dc grid response is almost the same for the DDE method, the dc-bus voltage response with the DDE method shows better damping and tracking behavior, as depicted in Fig. 14. It should be mentioned that the PMSG outer loop damper is sensitive to the load type variation, where the damping factor of the mechanical poles drops from 0.31 pu to 0.09 pu when the load type changes from 100% CPL to pure resistive.

E. DIFFERENT WIND SPEED PATTERN

A practical wind speed pattern based on real wind speed measurement [32], [33] is used to examine the robustness of the proposed stability enhancement options. The same test employed in Section V-B has been used, and the dc grid response is recorded for 600 s. Fig. 15 compares the responses of the AGS and DDE enhancement methods, both methods were able to preserve the system stability at different wind speed patterns, showing the same dynamic behavior obtained in Figs. 11-12. Moreover, the proposed controllers show a well-damped and stable response for a time interval of 10 minutes, proving the robustness of the proposed controllers to run for longer times.

F. DC-LINK VOLTAGE CONTROLLER BANDWIDTH VARIATION

For the same operating conditions in Figs. 11-14, the system response can be further improved by increasing the bandwidth (BW) of the dc-link voltage control loop. Increasing this BW is associated with modifying the controllers' gains of the proposed solutions. For the AGS method, the controller gain is increased by 1.75 pu; whereas for the dc damper method, the controller gain is increased by 1.3 pu. Figs. 16-17 show the dc grid response for both methods. For the ac grid support method (AGS-Fig. 16), it is obvious that the dc grid response is improved by increasing the bandwidth of the dc-link voltage loop, yielding in overshoots less than $\pm 0.2\%$ in the dc-link voltage response and reduction in the recovery time. A similar improvement in the dc grid response is obtained for the dc damper method (DDE-Fig. 17); it is clear that the dc-link voltage overshoots are reduced to less than $\pm 0.2\%$ with shorter recovery time.

VI. VALIDATION RESULTS

The validity of the proposed control strategy is verified by a hardware-in-the-loop (HIL) real-time simulation setup using the OPAL-RT OP5600 real-time simulation platform. The dc grid system investigated in Fig. 1 is simulated in real-time,

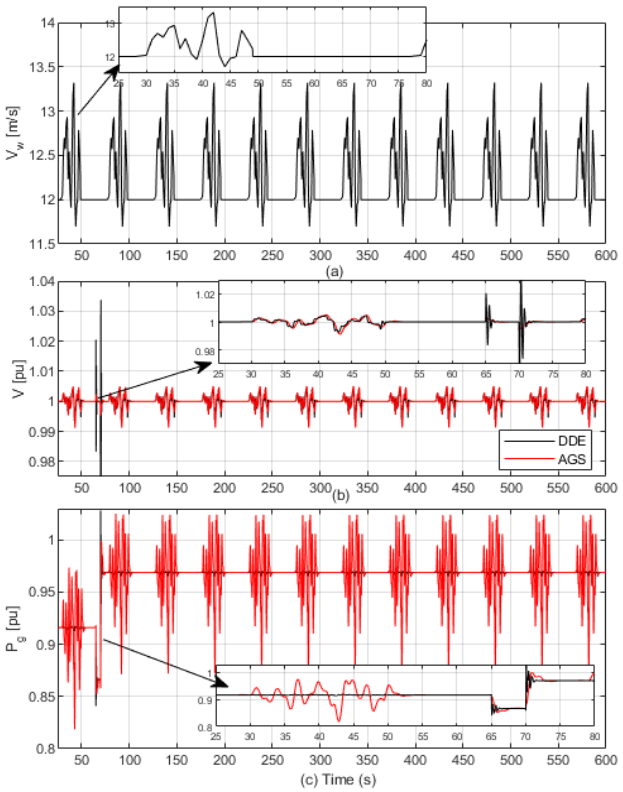

FIGURE 15. System response with AGS and DDE methods for 600s and different wind speed pattern (a) wind speed, (b) DC bus voltage, and (c) PMSG active power.

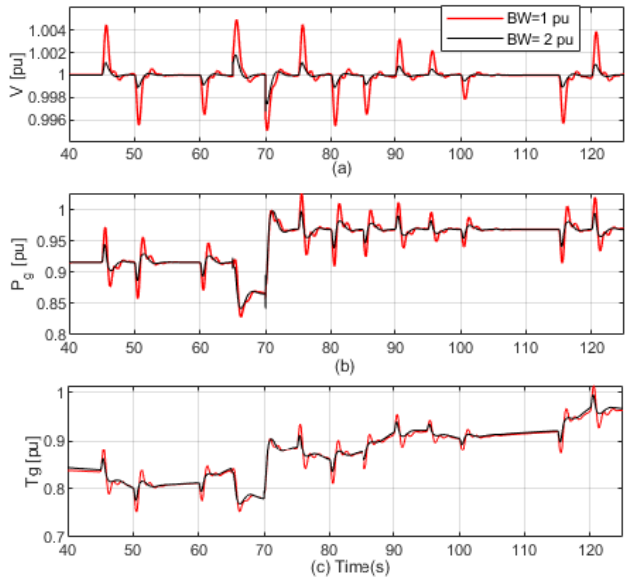

FIGURE 16. System response with AGS method under dc-link controller bandwidth variation. (a) DC bus voltage, (b) PMSG active power, and (c) PMSG Torque.

and the control system is implemented in real-time to test its real-time performance and implementation aspects. The results are captured on a four-channel 500-MHz oscilloscope

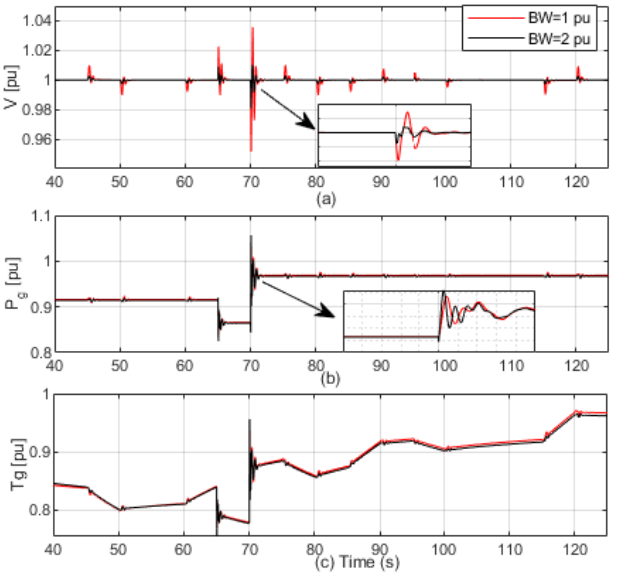

FIGURE 17. System response with DDE under dc-link controller bandwidth variation. (a) DC bus voltage, (b) PMSG active power, and (c) PMSG Torque.

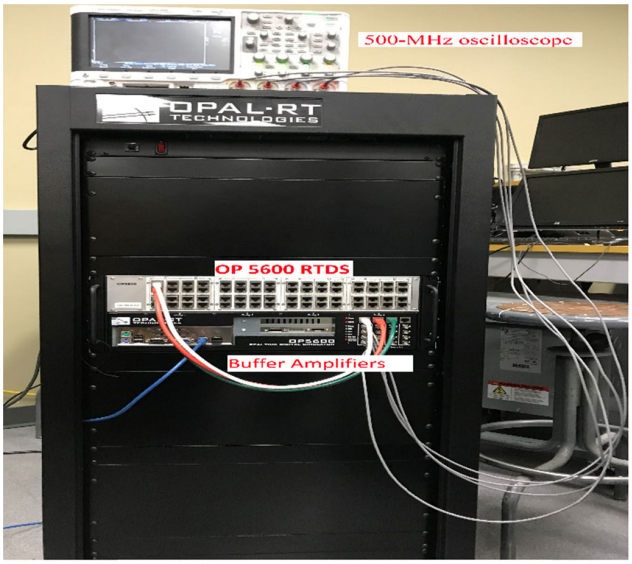

FIGURE 18. HIL tests setup.

connected to a data-acquisition card on a Virtex-6 FPGA board with a time step of 290 ns, as depicted in Fig. 18. The system performance with the proposed stability enhancement methods is evaluated at high- and low-wind speeds to examine the functionality of the stabilization strategies at different operating points; additionally, the CPL penetration level is set to 100%.

Figs. 20-21 show the dc grid response when the wind speed varies (see Fig. 19) for the ac grid support (AGS) and dc damper enhancement (DDE) methods, respectively. At rated wind speed (Fig. 20(a) and Fig. 21(a)), it can be seen that the system response on the HIL platform shows an

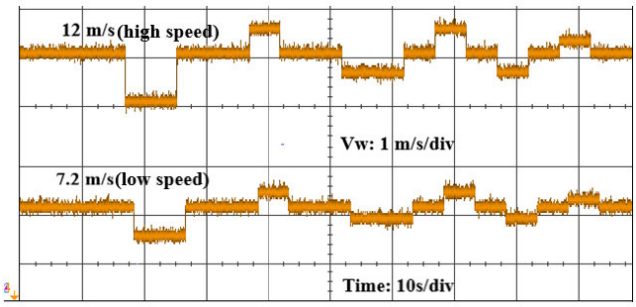

FIGURE 19. Wind speed profile for HIL simulations.

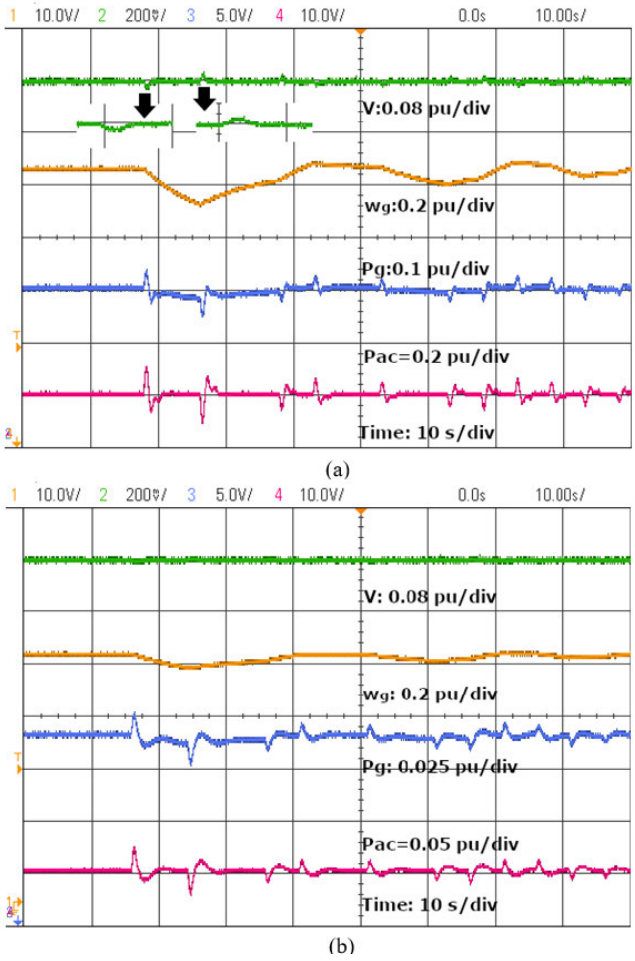

FIGURE 20. System response with AGS method (a) High-speed operation (b) low-speed operation.

excellent agreement with the time-domain nonlinear simulations results presented in Section V, where the grid-connected system shows a well-damped response against the wind speed variation with the AGS and DDE strategies. Furthermore, it is obvious that the proposed stability solutions are capable of preserving the system stability when the wind speed is low with the same design parameters (Fig. 20(b) and Fig. 21(b)). This proves the robustness of the selected

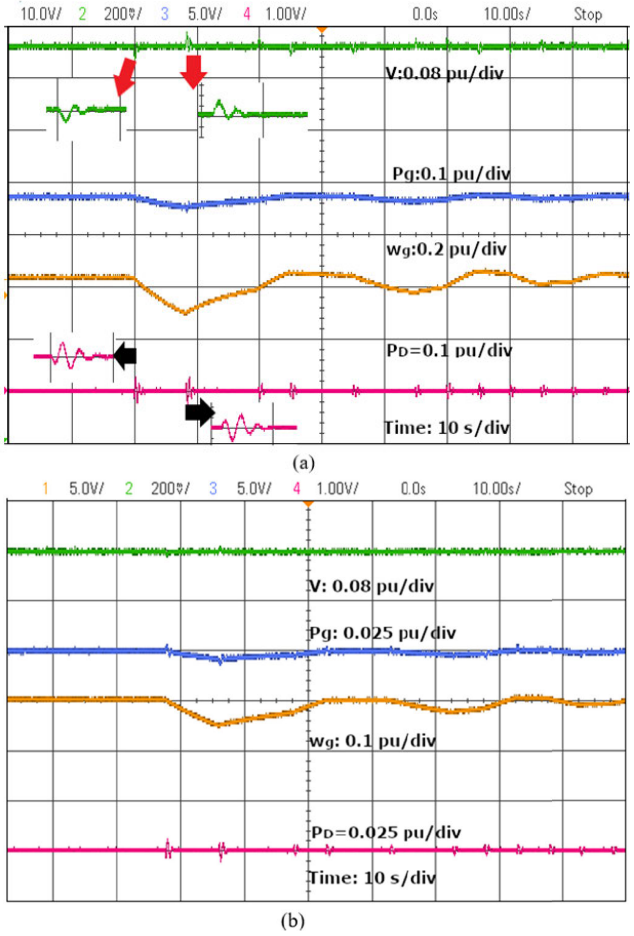

FIGURE 21. System response with DDE method (a) High-speed operation (b) low-speed operation.

compensators parameters against the variation of the wind turbine generator operating points.

VII. CONCLUSION

This paper presents a detailed modeling, comprehensive stability analysis, and stability enhancement methods for a dc grid with a high penetration level of wind power generation. It has been found that the wind turbine mechanical dynamics can significantly affect the system stability margins if the two-mass model is considered. With the PMSG active damper, it has been shown that the damping capability of the mechanical eigenvalues is remarkably affected by the load nature, and the system capacitance; whereas the dc feeder parameters have a minimal impact on the wind generator dynamics. Two stability enhancement methods have been discussed to address the instability problems from different aspects. First, the ac grid support method stabilizes the system via injecting power components from the ac grid, this method can preserve the system stability and is very robust against the dc grid uncertainties. Second, the dc damper method stabilizes the system via injecting stabilizing power components by an auxiliary unit. This method increases the system

stability margins, leading to satisfactory dynamic performance. The theoretical results are verified using detailed non-linear simulations and hardware-in-the-loop studies to validate the feasibility of hardware implementation.

VIII. RESEARCH STATUS

The research in this paper is initially developed as part of the Ph.D. research work of the first author [25]. A focused version of this research work is presented in this paper. The research is continued to study fault ride-through capability for the PMSG-based wind energy conversion system in dc grids.

APPENDIX

DC Distribution System Ratings: 1800 V, composite load rating 2.5 MW, dc feeder parameters: 16.4 mΩ/km, 39 μ H/km; $C_{Bus} = 20$ mF.

AC Grid and VSC: 2 MVA, 690 V, VSC filter parameters:300 μH, 6.5 mΩ, power control loop bandwidth = 600 rad/s, current control loop bandwidth = 800 Hz.

Wind Turbine PMSG: 2 MW, 690 V/11.25 Hz, $R_s = 0.00344$ pu, $L_d = 0.4026$ pu, $L_q = 0.7685$ pu, $H_g = 0.53$ s, $H_t = 4.27$ s, $P = 30$, $K_s = 1.6$ elec/pu.rad, $C_g = 24$ mF, $G_c(s) = 4.6 + 28/s$ pu, $G_{ac}(s) = 0.1 + 50/s$ pu, $G_{vdc}(s) = 0.6 + 24/s$ pu, $C_g = 24$ mF, $K = 20$ A/rad/s, damping factor = 2 pu, corner frequency = 10 rad/s.

AGS Parameters: $k_{ps} = 27$ kW/V, $k_{ps} = 3.14$ rad/s.

DDE Parameters: $C_{dc} = 50$ mF, $k_{ds} = 880$ pu, $,\xi_{ds} = 0.66$ pu, and $\omega_{ds} = 6.28$ rad/s.

REFERENCES

[1] B. Wang, M. Sechilariu, and F. Locment, "Intelligent DC microgrid with smart grid communications: Control strategy consideration and design," *IEEE Trans. Smart Grid*, vol. 3, no. 4, pp. 2148–2156, Dec. 2012.

[2] H. Lotfi and A. Khodaei, "AC versus DC microgrid planning," *IEEE Trans. Smart Grid*, vol. 8, no. 1, pp. 296–304, Jan. 2017.

[3] L. Xu and D. Chen, "Control and operation of a DC microgrid with variable generation and energy storage," *IEEE Trans. Power Del.*, vol. 26, no. 4, pp. 2513–2522, Oct. 2011.

[4] S.-Y. Lu, L. Wang, T.-M. Lo, and A. V. Prokhorov, "Integration of wind power and wave power generation systems using a DC microgrid," *IEEE Trans. Ind. Appl.*, vol. 51, no. 4, pp. 2753–2761, Jul. 2015.

[5] M. M. N. Amin and O. A. Mohammed, "DC-bus voltage control technique for parallel-integrated permanent magnet wind generation systems," *IEEE Trans. Energy Convers.*, vol. 26, no. 4, pp. 1140–1150, Dec. 2011.

[6] C. M. Jenisha, N. Ammasaigounden, N. Kumaresan, and K. Bhagyasri, "Power electronic interface with de-coupled control for wind-driven PMSG feeding utility grid and DC load," *IET Power Electron.*, vol. 11, no. 2, pp. 329–338, Feb. 2018.

[7] A. D. Hansen and G. Michalke, "Modelling and control of variable-speed multi-pole permanent magnet synchronous generator wind turbine," *Wind Energ.*, vol. 11, no. 5, pp. 537–554, Sep. 2008.

[8] M. F. M. Arani and Y. A.-R.-I. Mohamed, "Assessment and enhancement of a full-scale PMSG-based wind power generator performance under faults," *IEEE Trans. Energy Convers.*, vol. 31, no. 2, pp. 728–739, Jun. 2016.

[9] A. Hansen and G. Michalke, "Multi-pole permanent magnet synchronous generator wind turbines' grid support capability in uninterrupted operation during grid faults," *IET Renew. Power Gener.*, vol. 3, no. 3, p. 333, 2009.

[10] M. F. M. Arani and Y. A.-R.-I. Mohamed, "Analysis and damping of mechanical resonance of wind power generators contributing to frequency regulation," *IEEE Trans. Power Syst.*, vol. 32, no. 4, pp. 3195–3204, Jul. 2017.

[11] H. Geng, D. Xu, B. Wu, and G. Yang, "Active damping for PMSG-based WECS with DC-link current estimation," *IEEE Trans. Ind. Electron.*, vol. 58, no. 4, pp. 1110–1119, Apr. 2011.

[12] T. Ackermann, *Wind Power in Power Systems*, vol. 140. Hoboken, NJ, USA: Wiley, 2005.

[13] M. F. M. Arani and Y. A.-R.-I. Mohamed, "Analysis and mitigation of undesirable impacts of implementing frequency support controllers in wind power generation," *IEEE Trans. Energy Convers.*, vol. 31, no. 1, pp. 174–186, Mar. 2016.

[14] A. A. A. Radwan and Y. A.-R.-I. Mohamed, "Linear active stabilization of converter-dominated DC microgrids," *IEEE Trans. Smart Grid*, vol. 3, no. 1, pp. 203–216, Mar. 2012.

[15] M. Wu, D. D.-C. Lu, and C. K. Tse, "Direct and optimal linear active methods for stabilization of LC input filters and DC/DC converters under voltage mode control," *IEEE J. Emerg. Sel. Topics Circuits Syst.*, vol. 5, no. 3, pp. 402–412, Sep. 2015.

[16] A. Kwasinski and C. N. Onwuchekwa, "Dynamic behavior and stabilization of DC microgrids with instantaneous constant-power loads," *IEEE Trans. Power Electron.*, vol. 26, no. 3, pp. 822–834, Mar. 2011.

[17] L. Xing and J. Sun, "Optimal damping of multistage EMI filters," *IEEE Trans. Power Electron.*, vol. 27, no. 3, pp. 1220–1227, Mar. 2012.

[18] X. Liu, A. J. Forsyth, and A. M. Cross, "Negative input-resistance compensator for a constant power load," *IEEE Trans. Ind. Electron.*, vol. 54, no. 6, pp. 3188–3196, Dec. 2007.

[19] E. Jamshidpour, B. Nahid-Mobarakeh, P. Poure, S. Pierfederici, F. Meibody-Tabar, and S. Saadate, "Distributed active resonance suppression in hybrid DC power systems under unbalanced load conditions," *IEEE Trans. Power Electron.*, vol. 28, no. 4, pp. 1833–1842, Apr. 2013.

[20] X. Zhang, D. M. Vilathgamuwa, K.-J. Tseng, B. S. Bhangu, and C. J. Gajanayake, "Power buffer with model predictive control for stability of vehicular power systems with constant power loads," *IEEE Trans. Power Electron.*, vol. 28, no. 12, pp. 5804–5812, Dec. 2013.

[21] D. Chen, L. Xu, and J. Yu, "Adaptive DC stabilizer with reduced DC fault current for active distribution power system application," *IEEE Trans. Power Syst.*, vol. 32, no. 2, pp. 1430–1439, Mar. 2017.

[22] X. Zhang, X. Ruan, H. Kim, and C. K. Tse, "Adaptive active capacitor converter for improving stability of cascaded DC power supply system," *IEEE Trans. Power Electron.*, vol. 28, no. 4, pp. 1807–1816, Apr. 2013.

[23] X. Wang, F. Blaabjerg, M. Liserre, Z. Chen, J. He, and Y. Li, "An active damper for stabilizing power-electronics-based AC systems," *IEEE Trans. Power Electron.*, vol. 29, no. 7, pp. 3318–3329, Jul. 2014.

[24] L. Jia, X. Ruan, W. Zhao, Z. Lin, and X. Wang, "An adaptive active damper for improving the stability of grid-connected inverters under weak grid," *IEEE Trans. Power Electron.*, vol. 33, no. 11, pp. 9561–9574, Nov. 2018.

[25] A. M. I. Mohamad, "Modeling, dynamic analysis, and stabilization of active DC distribution systems," Ph.D. dissertation, Dept. Elect. Eng., Univ. Alberta., Edmonton, AB, Canada, 2018.

[26] K.-H. Kim, Y.-C. Jeung, D.-C. Lee, and H.-G. Kim, "LVRT scheme of PMSG wind power systems based on feedback linearization," *IEEE Trans. Power Electron.*, vol. 27, no. 5, pp. 2376–2384, May. 2012.

[27] X. Yuan, F. Wang, D. Boroyevich, Y. Li, and R. Burgos, "DC-link voltage control of a full power converter for wind generator operating in weak-grid systems," *IEEE Trans. Power Electron.*, vol. 24, no. 9, pp. 2178–2192, Sep. 2009.

[28] M. Davari and Y. A.-R.-I. Mohamed, "Robust DC-link voltage control of a full-scale PMSG wind turbine for effective integration in DC grids," *IEEE Trans. Power Electron.*, vol. 32, no. 5, pp. 4021–4035, May. 2017.

[29] A. Yazdani and R. Iravani, *Voltage-Sourced Converters in Power Systems*. New York, NY, USA: Wiley, 2010.

[30] A. M. I. Mohamad and Y. A.-R.-I. Mohamed, "Analysis and mitigation of interaction dynamics in active DC distribution systems with positive feedback islanding detection schemes," *IEEE Trans. Power Electron.*, vol. 33, no. 3, pp. 2751–2773, Mar. 2018.

[31] A. M. I. Mohamad and Y. A.-R.-I. Mohamed, "Investigation and enhancement of stability in grid-connected active DC distribution systems with high penetration level of dynamic loads," *IEEE Trans. Power Electron.*, vol. 34, no. 9, pp. 9170–9190, Sep. 2019.

[32] M. F. M. Arani and Y. A.-R.-I. Mohamed, "Analysis and impacts of implementing droop control in DFIG-based wind turbines on microgrid/weak-grid stability," *IEEE Trans. Power Syst.*, vol. 30, no. 1, pp. 385–396, Jan. 2015.

[33] E. Mosha, "Database of wind characteristics," DTU, Lyngby, Denmark, Tech. Rep., 2014, pp. 1–43. [Online]. Available: http://www.winddata.com

AHMED M. I. MOHAMAD was born in Cairo, Egypt, in July 1987. He received the B.Sc. (Hons.) and M.Sc. degrees in electrical engineering from Ain Shams University, Cairo, Egypt, in 2010 and 2014, respectively, and the Ph.D. degree in electrical engineering from the University of Alberta, Canada, in 2018. He is currently a Postdoctoral Fellow with the University of Alberta. His research interests are in the areas of dc grids, integration of renewable sources into distribution networks, and modeling and control of power electronic converters.

MOHAMMADREZA FAKHARI MOGHADDAM ARANI (Member, IEEE) received the B.Sc. degree from the Sharif University of Technology, Tehran, Iran, in 2009, the M.Sc. degree from the University of Waterloo, Waterloo, Canada, in 2012, and the Ph.D. degree from the University of Alberta, Edmonton, Canada, in 2017, all in electrical engineering. From 2012 to 2013, he was a Research Associate with the University of Waterloo. He was a NSERC Postdoctoral Fellow with the University of Toronto, Toronto, Canada, from 2017 to 2019. He joined Ryerson University as an Assistant Professor, in July 2019. His research interests include microgrids dynamics and control, cyber-physical security of smart grids, renewable and distributed generation, plug-in hybrid electric vehicles, power system stability, and power electronics.

YASSER ABDEL-RADY I. MOHAMED (Senior Member, IEEE) was born in Cairo, Egypt, in November 1977. He received the B.Sc. (Hons.) and M.Sc. degrees in electrical engineering from Ain Shams University, Cairo, in 2000 and 2004, respectively, and the Ph.D. degree in electrical engineering from the University of Waterloo, Waterloo, ON, Canada, in 2008.

He is currently a Professor with the Department of Electrical and Computer Engineering, University of Alberta, AB, Canada. His research interests include dynamics and controls of power converters, grid integration of distributed generation and renewable resources, microgrids, modeling, analysis and control of smart grids, and electric machines and motor drives.

Dr. Mohamed is an Associate Editor of the IEEE TRANSACTIONS ON POWER ELECTRONICS, and an Editor of the IEEE TRANSACTIONS ON POWER SYSTEMS, the IEEE TRANSACTIONS ON SMART GRID, and the IEEE POWER ENGINEERING LETTERS. He is a Registered Professional Engineer at the Province of Alberta.